

**NASA TECHNICAL
REPORT**



NASA TR R-296

C. 1

NASA TR R-296

LOAN COPY: RETURN TO
AFWL (WLIL-2)
KIRTLAND AFB, N MEX

0068463



TECH LIBRARY KAFB, NM

MULTIDIMENSIONAL GAS FLOW THROUGH PERMEABLE CHAR LAYERS AND ITS EFFECTS ON ABLATION

by Harold G. Bush and Marvin B. Dow

Langley Research Center

Langley Station, Hampton, Va.



MULTIDIMENSIONAL GAS FLOW THROUGH PERMEABLE CHAR LAYERS
AND ITS EFFECTS ON ABLATION

By Harold G. Bush and Marvin B. Dow

Langley Research Center
Langley Station, Hampton, Va.

NATIONAL AERONAUTICS AND SPACE ADMINISTRATION

For sale by the Clearinghouse for Federal Scientific and Technical Information
Springfield, Virginia 22151 - CFSTI price \$3.00

MULTIDIMENSIONAL GAS FLOW THROUGH PERMEABLE CHAR LAYERS AND ITS EFFECTS ON ABLATION

By Harold G. Bush and Marvin B. Dow
Langley Research Center

SUMMARY

A theoretical analysis of the pressure fields within the char layers of cylindrical and hemispherical ablation models is presented. The distribution over the surface of mass flow from the char layer is given for both geometries. These multidimensional mass-flow distributions show that gas flow through the char layer can be significantly different from the one-dimensional assumption previously used by ablation analysts. Further, the theoretical results show that it is possible for the external pressure field to cause gas flow into the char layer, in which case the diffusion of energy and oxygen through the boundary layer to the material surface is increased.

The appropriate analytical results were used to modify an existing one-dimensional ablation computer program to make convective blocking at the ablator surface responsive to the major parameters governing mass flow through permeable char layers. A comparison of analytical and experimental results shows that ablation performance can be significantly affected by multidimensional mass flow through the char layer.

INTRODUCTION

An important heat-shielding mechanism of charring ablators is the blocking of convective heating by pyrolysis gas injection into the boundary layer. Analytical ablation models, such as that in reference 1, considered the transverse thermal and pressure gradient to be negligible in comparison with gradients through the material thickness. Thus, heat and mass transfer were restricted to one-dimensional treatments. Specifically, for convective-blocking purposes, pyrolysis gases were assumed to be injected into the boundary layer at the same body location where they were generated, independent of the external pressure field.

Although the assumption of one-dimensional gas flow through the char layer is justifiable for many applications, the correctness of this assumption becomes questionable in the analysis of ablation performance of small ground-test models subjected to high-pressure environments or materials which form highly permeable chars. Inasmuch as the char layer is permeable in all directions, gases will respond to the external or

internal pressure field by following the path of least resistance. In fact, instead of gases flowing outward from the char surface to decrease convective heating, the possibility exists for gas inflow to occur at the char surface which will cause increased convective heating (ref. 2) and increased surface oxidation since oxygen diffusion through the boundary layer is affected by convective blocking in the same manner as is energy diffusion.

In this investigation the manner in which convective blocking is affected by multidimensional gas flow within the char is qualitatively determined by characterizing the gas flow field within an idealized, permeable char layer. Multidimensional effects on convective blocking are related to ablation by comparison of experimental results with approximate calculations of ablation performance.

SYMBOLS

The units used for the physical quantities defined in this paper are given in the International System of Units (ref. 3).

C	stream concentration of oxygen by mass
h	stream enthalpy, J/kg
J_0, J_1	zero- and first-order Bessel functions, respectively
M	molecular weight, kg/mole
\dot{m}	mass flow rate, kg/m ² -s
P_m	Legendre polynomial
p	pressure, N/m ²
\dot{q}	cold-wall laminar convective heating rate, W/m ²
R	maximum radius of cylinder or hemisphere, m
R_0	interface location of hemisphere, m
r, θ, z	cylindrical coordinate system
r, φ, θ	spherical coordinate system

r_{ref}	reference radius, m
s	meridional distance, m
T	temperature, °K
t	char thickness, m
V	gas velocity, m/s
α	surface curvature parameter, cylinder radius/spherical nose radius
β	universal gas constant, J/°K-mole
β_n	nth root of $J_0(\beta_n) = 0$
γ_1, γ_2	geometric coefficients defined by equations (13a) and (13b)
η_1, η_2	geometric coefficients defined by equations (21a) and (21b)
ξ_1, ξ_2	approximate geometric coefficients (fig. 18)
κ	char permeability, m ²
μ	viscosity, N-s/m ²
ρ	density, kg/m ³
τ	shear stress, N/m ²
ψ	parameter equal to $\frac{M\kappa}{2\beta T\mu}$, m ² -s/N
ψ_p	parameter equal to $\frac{M_p\psi}{M}$, m ² -s/N
ψ_{bl}	parameter equal to $\frac{M_{bl}\psi}{M}$, m ² -s/N

Subscripts:

aero corrected for hot-wall and transpiration effects

bl	boundary layer
f	flight vehicle
g	ground-test model
max	maximum value
p	pyrolysis gases
r,z	component in the r or z direction, respectively
s	stagnation point
w	value at wall

ANALYSIS

The derivation and solution of the equations governing the gas pressure and flow fields within a permeable char layer are obtained for both a flat-faced cylinder and a hemisphere in the analysis which follows. In this analysis, the virgin material is assumed to be impermeable; thus, all pyrolysis gases injected at the interface of the char and virgin material transpire through the char layer only. This assumption is also valid for permeable virgin materials which form an impermeable seal at the interface during pyrolysis.

Conservation of mass in steady flow requires that

$$\text{div}(\rho V) = \nabla \cdot (\rho V) = 0 \quad (1)$$

According to Darcy's law (ref. 4), the fluid velocity in any direction is proportional to the pressure gradient in that direction and may be written

$$V = - \frac{\kappa}{\mu} \text{grad}(p) = - \frac{\kappa}{\mu} \nabla(p) \quad (2)$$

The fluid density is obtained from the ideal-gas equation of state, which is

$$\rho = \frac{pM}{\beta T} \quad (3)$$

Combining equations (1) to (3) yields

$$\nabla \cdot [\psi \nabla(p^2)] = 0 \quad (4)$$

where

$$\psi = \frac{M\kappa}{2\beta T\mu} \quad (4a)$$

It is recognized that the parameter ψ varies during the ablation process. However, multidimensional solutions of equation (4), assuming ψ variable, can be obtained only numerically. Since the purpose herein is to determine qualitatively those trends in gas flow through permeable char layers which are related to multidimensional or geometric effects, it is considered sufficient to assume as a first approximation that ψ is constant. In this case analytical solutions are possible since equation (4) reduces to

$$\nabla^2(p^2) = 0 \quad (5)$$

and is the governing equation for the pressure distribution within a permeable material.

Solutions for Cylindrical Char

The cylindrical coordinate systems and geometry used are shown in figure 1. For the rotationally symmetric problem $\frac{\partial}{\partial \theta} = 0$, equation (5) becomes

$$\frac{1}{r} \frac{\partial}{\partial r} \left(r \frac{\partial p^2}{\partial r} \right) + \frac{\partial^2 p^2}{\partial z^2} = 0 \quad (6)$$

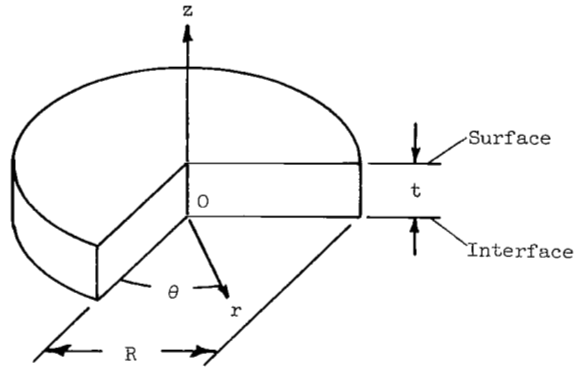


Figure 1.- Cylindrical coordinate system and geometry.

The boundary conditions chosen to represent a uniform-thickness char layer are

$$\frac{\partial p^2(r,0)}{\partial z} = - \frac{\dot{m}_p(r)}{\psi} \quad (z = 0) \quad (7a)$$

$$p^2(r,t) = p^2(r) \quad (z = t) \quad (7b)$$

$$\frac{\partial p^2(0,z)}{\partial r} = 0 \quad (r = 0) \quad (7c)$$

$$p^2(R,z) = p^2(R) = \text{Constant} \quad (r = R) \quad (7d)$$

The methods of separation of variables and superposition lead to the Fourier-Bessel series solution:

$$\begin{aligned}
p^2(r, z) = p^2(R) + \sum_{n=1}^{\infty} \frac{2}{R^2} \left\{ \int_0^R r J_0\left(\beta_n \frac{r}{R}\right) [p^2(r) - p^2(R)] dr \right\} \frac{J_0\left(\beta_n \frac{r}{R}\right) \cosh\left(\beta_n \frac{z}{R}\right)}{J_1^2(\beta_n) \cosh\left(\beta_n \frac{t}{R}\right)} \\
+ \sum_{n=1}^{\infty} \frac{2}{\psi R} \left[\int_0^R r J_0\left(\beta_n \frac{r}{R}\right) \dot{m}_p(r) dr \right] \left[\frac{\cosh\left(\beta_n \frac{z}{R}\right)}{\cosh\left(\beta_n \frac{t}{R}\right)} - \frac{\sinh\left(\beta_n \frac{z}{R}\right)}{\sinh\left(\beta_n \frac{t}{R}\right)} \right] \frac{J_0\left(\beta_n \frac{r}{R}\right) \sinh\left(\beta_n \frac{t}{R}\right)}{\beta_n J_1^2(\beta_n)}
\end{aligned} \quad (8)$$

The pressure-field solution, given by equation (8), is in general form. Various distributions of external pressure and pyrolysis mass injection may be imposed by performing the integration required in equation (8). The distribution of mass flow normal to and at the char layer surface $z = t$ is of primary interest and is given by

$$\dot{m}_w(r, t) = \rho V_z = -\psi \left(\frac{\partial p^2}{\partial z} \right)_{z=t} \quad (9)$$

Performing the operation on equation (8) as required by equation (9) yields

$$\begin{aligned}
\dot{m}_w(r, t) = \psi \left(\sum_{n=1}^{\infty} \frac{2}{\psi R^2} \left[\int_0^R r J_0\left(\beta_n \frac{r}{R}\right) \dot{m}_p(r) dr \right] \frac{J_0\left(\beta_n \frac{r}{R}\right)}{J_1^2(\beta_n) \cosh\left(\beta_n \frac{t}{R}\right)} \right. \\
\left. - \sum_{n=1}^{\infty} \frac{2}{R^3} \left\{ \int_0^R r J_0\left(\beta_n \frac{r}{R}\right) [p^2(r) - p^2(R)] dr \right\} \frac{\beta_n J_0\left(\beta_n \frac{r}{R}\right) \tanh\left(\beta_n \frac{t}{R}\right)}{J_1^2(\beta_n)} \right) \quad (10)
\end{aligned}$$

Evaluation of the integrals in equation (10) requires selection of external pressure and pyrolysis mass injection distributions. The experimentally determined pressure distribution from reference 5 for a flat-faced cylinder in high-speed flow is shown in figure 2. The pressure on the cylindrical surface $r = R$ is assumed to be constant and equal to the pressure on the face at the corner.

It is assumed that the mass injection distribution along the pyrolysis interface $z = 0$ is

$$\dot{m}_p(r, 0) = \text{Constant} = \dot{m}_p \quad (11)$$

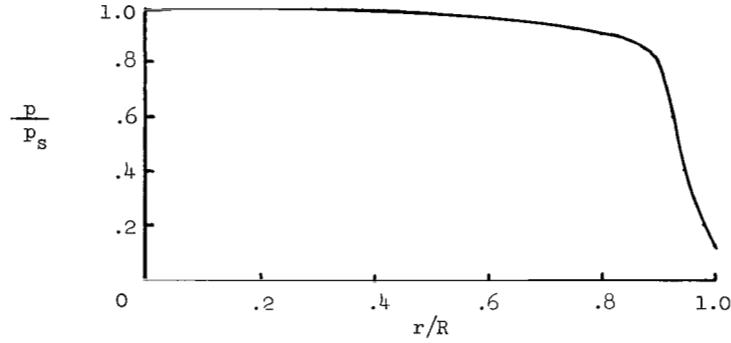


Figure 2.- Pressure distribution on a flat-faced cylinder.

Combining equations (10) and (11) yields

$$\dot{m}_w(r,t) = \gamma_1 \dot{m}_p - \gamma_2 \frac{\psi p_s^2}{R} \quad (12)$$

where

$$\gamma_1 = \sum_{n=1}^{\infty} \frac{2}{R^2} \left[\int_0^R r J_0\left(\beta_n \frac{r}{R}\right) dr \right] \frac{J_0\left(\beta_n \frac{r}{R}\right)}{J_1^2(\beta_n) \cosh\left(\beta_n \frac{t}{R}\right)} \quad (13a)$$

$$\gamma_2 = \sum_{n=1}^{\infty} \frac{2}{R^2} \left\{ \int_0^R r J_0\left(\beta_n \frac{r}{R}\right) \left[\frac{p^2(r) - p^2(R)}{p_s^2} \right] dr \right\} \frac{\beta_n J_0\left(\beta_n \frac{r}{R}\right) \tanh\left(\beta_n \frac{t}{R}\right)}{J_1^2(\beta_n)} \quad (13b)$$

The mass flow in the z -direction at the char surface, given by equation (12), is composed of two parts which are both functions of radial location r/R and the char thickness parameter t/R . The first term on the right-hand side of equation (12) is independent of the external pressure distribution whereas the second is independent of the pyrolysis gas injection rate. The influence of each term is discussed separately.

Effect of pyrolysis gas injection.- Figure 3 shows the mass flow distribution at the char surface $z = t$ resulting from pyrolysis gas injection along the interface, without the influence of external pressure gradients. The influence of the char edge at $r = R$ on mass flow from the surface $z = t$ is also shown in figure 3. The decrease in mass flow from the surface $z = t$ as t/R is increased is due to the greater amount of gas

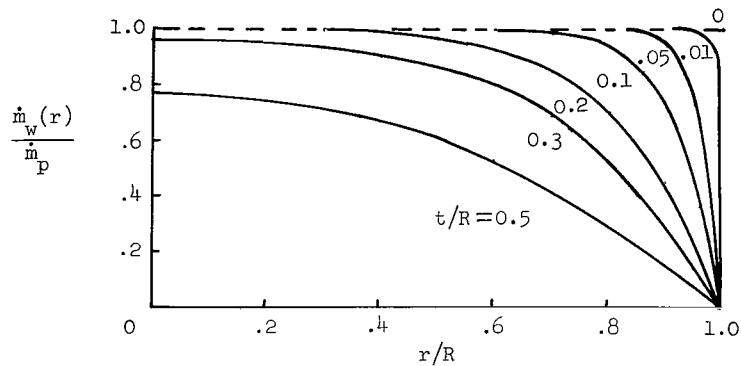


Figure 3.- Mass flow distribution at surface of cylindrical char layer resulting from pyrolysis gas injection at interface, without the influence of external pressure gradients.

which flows radially and escapes from the char edge $r = R$. However, relatively large values of t/R are required before mass flow at the stagnation point $r = 0$ is significantly reduced. Because ψ was assumed to be invariant with respect to the spatial coordinates, the results shown in figure 3 are independent of that parameter. One important case encompassed by this assumption is the isothermal flow of an ideal gas through an isotropically permeable material. In this case, the results shown in figure 3 are independent of the state and nature of the gas flowing and are valid for all values of char permeability except zero.

Effect of external pressure distribution.- Figure 4 shows the mass flow distribution at the char surface resulting from the external pressure distribution shown in figure 2 without the influence of pyrolysis gas injection. Mass flow into the stagnation region $r \approx 0$ is low but increases as t/R increases. The extreme variation in mass flow at $r/R \approx 0.9$ resulted from the abrupt decrease in the pressure distribution shown in figure 2 at the same location. If the pressure distribution were more "rectangular," the effect would be to decrease inflow over most of the surface and to move the point of maximum inflow to $r/R = 1$. Note that increased values of ψ and/or pressure or decreased body size cause increased inflow over most of the char surface.

Combined effects for cylindrical char.- The combined effects of the pyrolysis gas injection and external pressure distributions shown previously on mass flow through a cylindrical char layer are shown in figures 5(a) and 5(b). The figures show the ratio of mass flow from the char surface to that injected at the interface \dot{m}_w/\dot{m}_p as a function of surface location and char thickness. Figures 5(a) and 5(b) were calculated for values of $\frac{\psi p_s^2}{\dot{m}_p R} = 0.1$ and 1.0, respectively, to show the trend in mass flow through the char surface with that parameter since it is not constant during an ablation test and may vary over

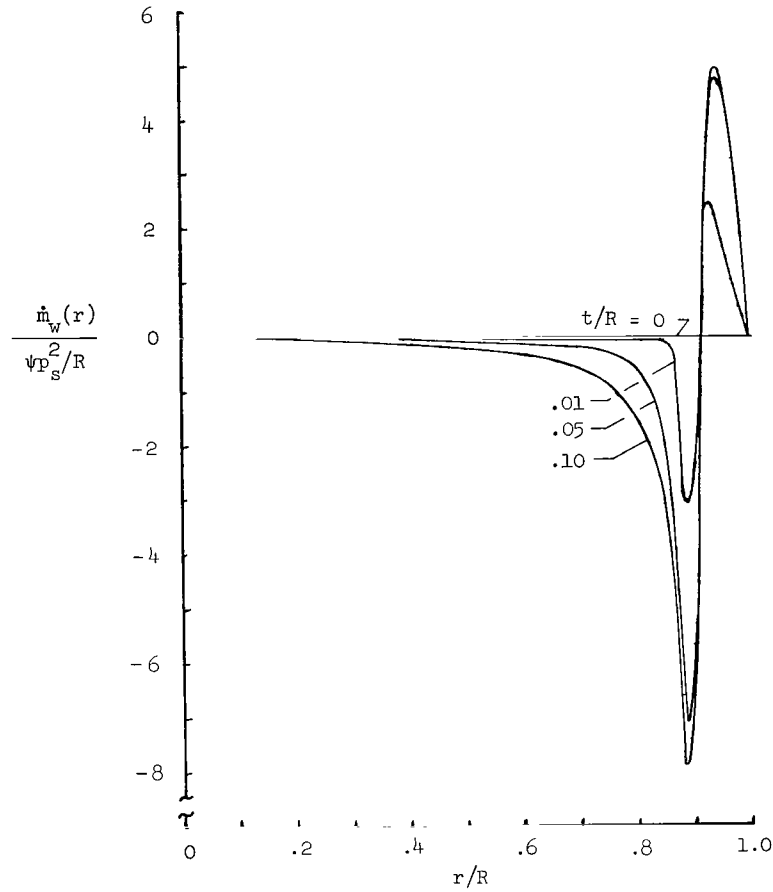
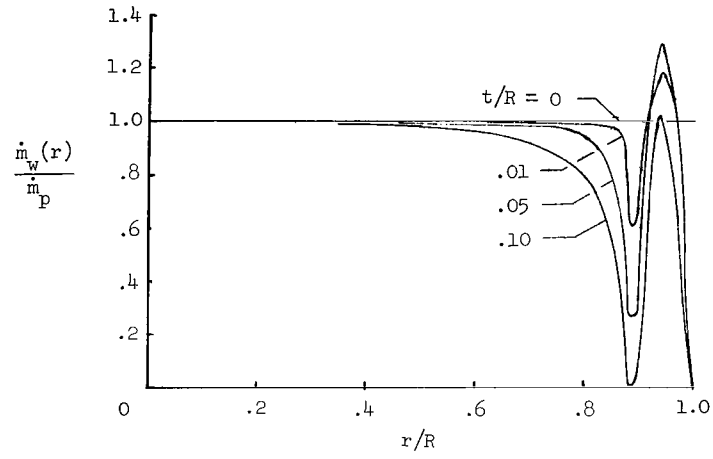


Figure 4.- Mass flow distribution at surface of cylindrical char layer resulting from external pressure distribution, without the influence of pyrolysis gas injection at the interface.

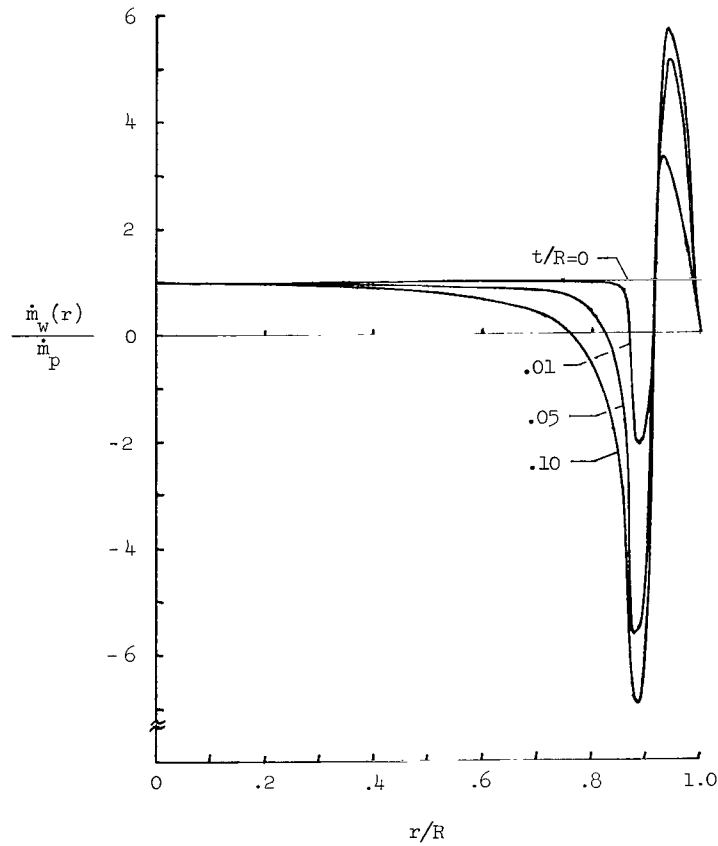
several orders of magnitude. For $t/R = 0$, mass flow from the surface is independent of radial location. However, as t/R is increased, inflow or greatly decreased outflow occurs at $r/R \approx 0.9$, whereas at the stagnation point $r = 0$, the mass flow is only slightly affected for the conditions shown. A comparison of figures 5(a) and 5(b) shows that the larger value of $\psi p_s^2 / \dot{m}_p R$ results in large inflow rates at $r/R \approx 0.9$. It is noted that even for the low value of $\psi p_s^2 / \dot{m}_p R$, increased char thickness t/R leads to decreased outflow or possibly inflow.

Solutions for Hemispherical Char

The spherical coordinate system and geometry used for the hemispherical char are shown in figure 6. For the rotationally symmetric problem $\frac{\partial}{\partial \theta} = 0$, equation (5) becomes



(a) $\frac{\psi p_s^2}{\dot{m}_p R} = 0.1.$



(b) $\frac{\psi p_s^2}{\dot{m}_p R} = 1.0.$

Figure 5.- Mass flow distribution at surface of cylindrical char layer resulting from pyrolysis gas injection and external pressure distribution.

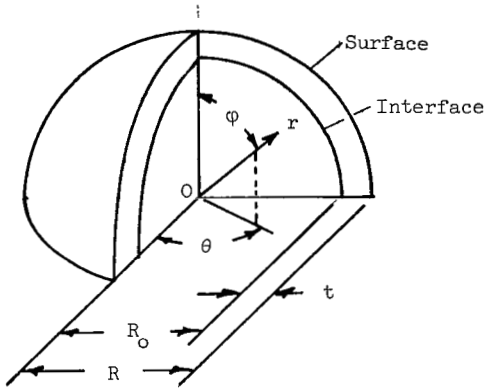


Figure 6.- Spherical coordinate system and geometry.

$$\frac{\partial}{\partial r} \left(r^2 \frac{\partial p^2}{\partial r} \right) + \frac{1}{\sin \varphi} \frac{\partial}{\partial \varphi} \left(\sin \varphi \frac{\partial p^2}{\partial \varphi} \right) = 0 \quad (14)$$

The boundary conditions selected for the hemispherical char layer are

$$\frac{\partial p^2(R_0, \varphi)}{\partial r} = - \frac{\dot{m}_p(\varphi)}{\psi} \quad (r = R_0) \quad (15a)$$

$$p^2(R, \varphi) = p^2(\varphi) \quad (r = R) \quad (15b)$$

$$\frac{\partial p^2(r, 0)}{\partial \varphi} = 0 \quad (\varphi = 0) \quad (15c)$$

$$\frac{\partial p^2(r, \frac{\pi}{2})}{\partial \varphi} = 0 \quad \left(\varphi = \frac{\pi}{2} \right) \quad (15d)$$

The boundary condition given by equation (15d) requires that there be no mass flow in the meridional direction at $\varphi = \pi/2$. In an actual case, the char layer would be continuous in the meridional direction at $\varphi = \pi/2$ and gas flow across this boundary could occur. However, this mass flow magnitude would be very small and should not significantly affect mass flow distributions at the surface for $\varphi < \pi/2$.

The methods of separation of variables and superposition lead to the Fourier-Legendre series solution

$$p^2(r, \varphi) = \sum_{m=0,2,4}^{\infty} \frac{\left[\left(\frac{r}{R_0} \right)^m + \frac{m}{m+1} \left(\frac{R_0}{r} \right)^{m+1} \right] \left[\int_0^{\pi/2} p^2(\varphi) P_m(\cos \varphi) \sin \varphi d\varphi \right] P_m(\cos \varphi)}{\left[\left(\frac{R}{R_0} \right)^m + \frac{m}{m+1} \left(\frac{R_0}{R} \right)^{m+1} \right] \left\{ \int_0^{\pi/2} [P_m(\cos \varphi)]^2 \sin \varphi d\varphi \right\}}$$

$$- \sum_{m=0,2,4}^{\infty} \frac{\frac{R_0}{\psi} \left[\left(\frac{r}{R} \right)^m - \left(\frac{R}{r} \right)^{m+1} \right] \left[\int_0^{\pi/2} \dot{m}_p(\varphi) P_m(\cos \varphi) \sin \varphi d\varphi \right] P_m(\cos \varphi)}{\left[m \left(\frac{R_0}{R} \right)^m + (m+1) \left(\frac{R}{R_0} \right)^{m+1} \right] \left\{ \int_0^{\pi/2} [P_m(\cos \varphi)]^2 \sin \varphi d\varphi \right\}} \quad (16)$$

The pressure-field solution, given by equation (16), is in general form. Particular solutions may be obtained by evaluating the integrals appearing therein. The Newtonian pressure distribution shown in figure 7 was selected for the hemisphere and is given by

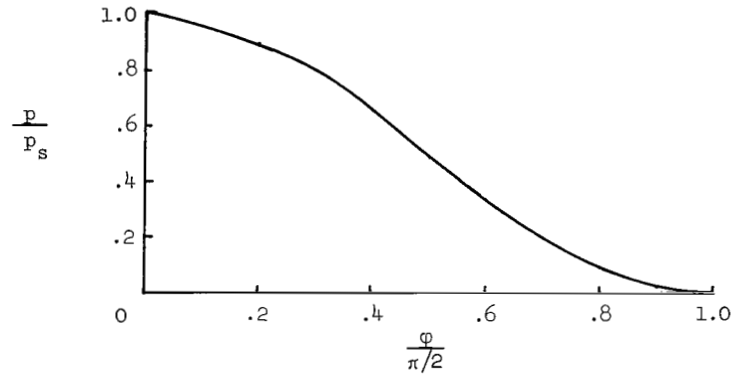


Figure 7.- Pressure distribution on a hemisphere.

$$\frac{p(\phi)}{p_s} = \cos^2 \phi \quad (17)$$

The mass injection rate along the interface $r = R_0$ was assumed to be

$$\dot{m}_p(R_0, \phi) = \text{Constant} = \dot{m}_p \quad (18)$$

The mass flow distribution normal to and at the char surface $r = R$ is given by

$$\dot{m}_w(R, \phi) = \rho V_r = -\psi \left(\frac{\partial p^2}{\partial r} \right)_{r=R} \quad (19)$$

Combining equations (16) to (19) yields

$$\dot{m}_w(R, \phi) = \eta_1 \dot{m}_p - \eta_2 \frac{\psi p_s^2}{R} \quad (20)$$

where

$$\eta_1 = \left(1 - \frac{t}{R} \right)^2 \quad (21a)$$

$$\eta_2 = \frac{8}{7} \left[\frac{1 - \left(1 - \frac{t}{R} \right)^5}{1 + \frac{2}{3} \left(1 - \frac{t}{R} \right)^5} \right] \left(\frac{3}{2} \cos^2 \phi - \frac{1}{2} \right) + \frac{32}{35} \left[\frac{1 - \left(1 - \frac{t}{R} \right)^9}{1 + \frac{4}{5} \left(1 - \frac{t}{R} \right)^9} \right] \left(\frac{35}{8} \cos^4 \phi - \frac{15}{4} \cos^2 \phi + \frac{3}{8} \right) \quad (21b)$$

The mass flow normal to the hemisphere surface, given by equation (20), is composed of two parts which are both functions of the char thickness parameter t/R . However, as in the case of the cylinder, the effects of pyrolysis gas injection and external pressure distribution can be considered separately.

Effect of pyrolysis gas injection.- Figure 8 shows the mass flow distribution at the char surface resulting from pyrolysis gas injection at the interface $r = R_0$ without the influence of external pressure gradients. From equations (20) and (21a), it can be seen that mass flow from the char surface is independent of meridional location φ and varies only with t/R . This condition occurs because there is no lateral flow at $\varphi = 0$ and $\varphi = \pi/2$. Because mass flow is in a radial direction, the area through which the pyrolysis gases transpire increases and, hence, the mass flow rate at the surface is less than that at the interface. As shown in figure 8, the reduction in mass flow rate at the stagnation point $\varphi = 0$ is much greater for the hemisphere than for the flat-faced cylinder (fig. 3) for the same value of t/R . As with the cylinder, when the isothermal flow of an ideal gas through an isotropically permeable material is considered, the results shown in figure 8 are valid for all values of char permeability except zero.

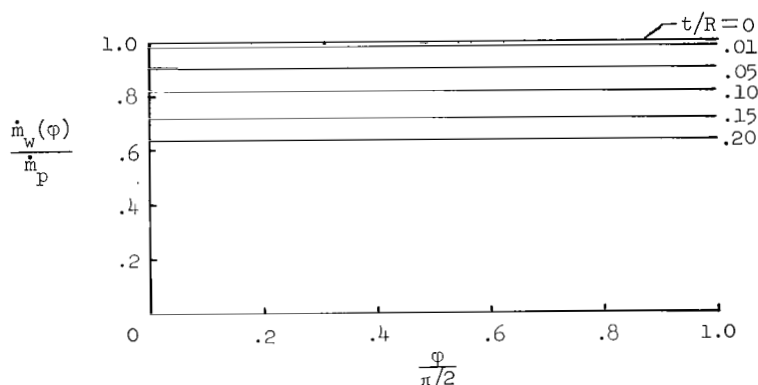


Figure 8.- Mass flow distribution at surface of hemispherical char layer resulting from pyrolysis gas injection at interface, without the influence of external pressure gradients.

Effect of external pressure distribution.- Figure 9 shows the mass flow distribution at the hemisphere surface resulting from the external pressure distribution without the influence of pyrolysis gas injection. Inflow (negative values of $\frac{\dot{m}_w(\varphi)}{\psi p_s^2/R}$) occurs in the stagnation region $\varphi < 0.68$ and outflow occurs for larger values of φ . Also, mass flow into the stagnation region increases with increasing t/R . Note from the ordinate parameter that large values of ψ and/or pressure or small values of body size lead to increased inflow in the stagnation vicinity.

Combined effects for hemispherical char.- The combined effects of pyrolysis gas injection and external pressure distribution on mass flow through a hemispherical char layer are shown in figures 10(a) and 10(b). The figures show the mass flow ratio \dot{m}_w/\dot{m}_p as a function of surface location and char thickness. Data for figures 10(a) and 10(b) were calculated using values of $\frac{\psi p_s^2}{\dot{m}_p R} = 0.1$ and 1.0, respectively, to show the trend

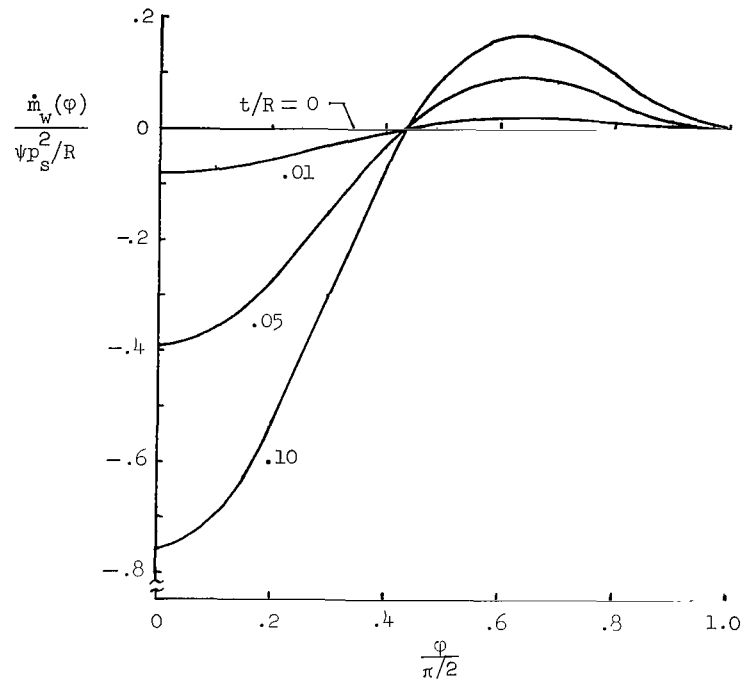
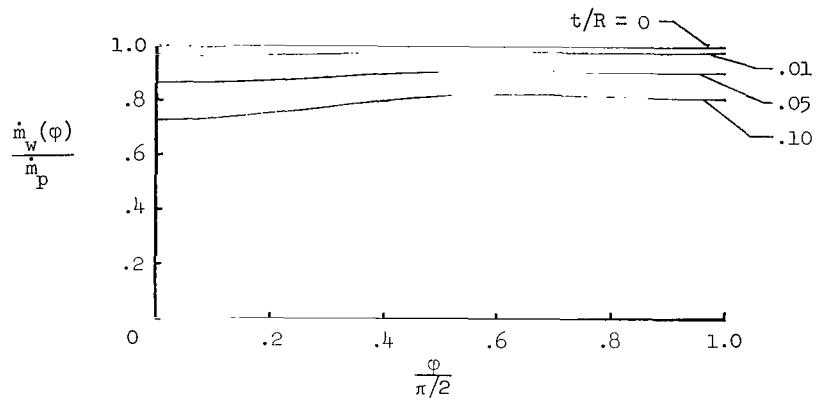


Figure 9.- Mass flow distribution at surface of hemispherical char layer resulting from external pressure distribution, without the influence of pyrolysis gas injection at the interface.

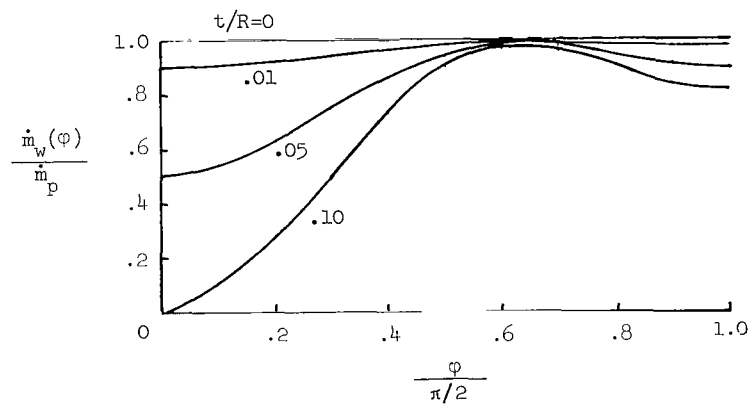
in mass flow through the char surface with that parameter since, as stated previously, it is not constant during an ablation test and may vary over several orders of magnitude. For the low value of $\psi p_s^2/\dot{m}_p R$, the mass flow ratio is relatively independent of meridional location and decreases as t/R is increased. However, for the larger value of $\psi p_s^2/\dot{m}_p R$ the mass flow ratio is strongly dependent on meridional location with significant reductions in mass flow from the char surface occurring in the stagnation vicinity for increased values of char thickness.

Comparison of Cylindrical and Hemispherical Char Results

Comparing figures 5 and 10 and considering equal values of t/R shows that mass flow from the surface of the two geometries is significantly different except for $t/R = 0$. At the stagnation point, which is usually the point of interest in ground tests, mass flow from the hemisphere is more greatly reduced at a given value of char thickness than from the cylinder. Thus, surface curvature, although undefined herein except for the extreme cases considered, has a detrimental effect on convective blocking at the stagnation point of a body. Therefore, hemispheres or small ground-test models with highly curved faces are more susceptible to the effects of multidimensional flow through the



(a) $\frac{\psi p_s^2}{\dot{m}_p R} = 0.1$



(b) $\frac{\psi p_s^2}{\dot{m}_p R} = 1.0$

Figure 10.- Mass flow distribution at surface of hemispherical char layer resulting from pyrolysis gas injection and external pressure distribution.

char layer at the stagnation point than flat-faced models are. Thus, material ablation performance, determined experimentally using hemispherical or highly curved ground-test models, may be significantly different from that which would occur in flight on a larger body where effects of multidimensional mass flow would be diminished.

However, convective blocking on the surface of the cylindrical char is severely affected over a narrow region near the edge $r/R = 1$. The loss of convective blocking near the edge $r/R \approx 0.9$ may be the cause of shape change which some flat-faced ablation models undergo during convective heating in a high-speed thermal environment. Shape change resulting from greatly reduced convective blocking near the edge will change the external pressure distribution which, in turn, will result in a less severe inflow condition through the char surface. This effect is illustrated in a subsequent section of this paper by evaluating mass flow through a cylindrical char resulting from a less "rectangular" pressure distribution than that shown in figure 2.

The effect of mass transfer on convective heating is shown in figure 11, which was computed by using the theory of reference 6. It was considered, heretofore, that the outflow portion of figure 11 typified charring-ablator performance. However, the possibility of inflow at the char surface has been shown to exist, in which case the diffusion rates of energy and oxygen through the boundary layer to the ablator surface are increased as shown in figure 11.

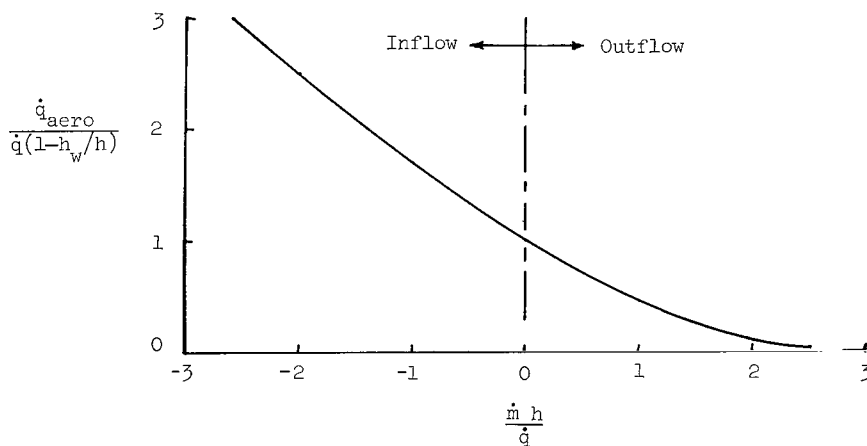


Figure 11.- Effect of mass transfer on convective heating to a surface (laminar boundary layer).

COMPARISON OF EXPERIMENTAL AND CALCULATED ABLATION PERFORMANCE

The foregoing analytical results show that in certain situations mass flow within char layers can be multidimensional. However, these analytical results (for example, figs. 5 and 10, etc.) are insufficient by themselves to determine the effects of multidimensional flow on ablation performance. Such effects can only be determined analytically through ablation calculations. In order to perform the desired calculations, an existing ablation computer program was modified to incorporate the analytical results presented in the preceding sections. Details of this modification are given in appendix A. This modification made convective blocking in the analytical ablation model responsive to the major parameters which affect gas flow through permeable chars, namely, external pressure, char thickness, body size, and permeability. Ablation calculations performed with the modified computer program are presented solely to illustrate the trends in predicted material performance when multidimensional flow through the char is considered.

In ablation tests conducted at the Langley Research Center, prior to the analysis herein, two low-density phenolic-nylon (LDPN) materials were subjected to high-pressure thermal environments. Details of this test program are given in appendix B. It was found that the material which had the greater char permeability was significantly more affected by the test environment than was the other. A representative series of those tests was selected for comparison with ablation calculations to illustrate the effect of multidimensional mass flow within the char layer on ablation performance.

Each test result was computed by two methods. The first method considered one-dimensional mass flow (ODF) through the char layer as described in reference 1. The second method considered multidimensional mass flow (MDF) through the char layer as described in appendix A. Both ODF and MDF calculations used the same cold-wall heating-rate history corrected for shape changes which occurred during the corresponding test. With the exception of char permeability and density, all physical constants and material properties were the same for all calculations for both materials and are given in table I. Char permeability and density values used for calculations of each test result are indicated in the appropriate figures which follow. All calculations used values of ψ_p/κ and ψ_{bl}/κ equal to 6 and 18×10^{-3} s/N, respectively.

Material A

As described in appendix B, material A was the more adversely affected of the two low-density phenolic-nylon materials tested. Results of tests of material A at a nominal stagnation pressure of 2.7 atmospheres (2.74×10^5 newtons/m²) were selected for comparison with calculations. The dashed curve in figure 12 connects experimentally

Curve (a)	C = 0.038		C = 0.115		C = 0.232	
	$\rho, \text{kg/m}^3$	κ, m^2	$\rho, \text{kg/m}^3$	κ, m^2	$\rho, \text{kg/m}^3$	κ, m^2
ODF	256	—	256	—	256	—
MDF-1 ^b	256	6.5×10^{-11}	256	6.5×10^{-11}	256	6.5×10^{-11}
MDF-2 ^b	214	16	214	16	256	6.5
MDF-3 ^c	214	16	214	16	256	6.5

^aAblation calculations performed assuming one-dimensional mass flow in the char layer are denoted by ODF, whereas those performed assuming multidimensional mass flow in the char are denoted by MDF.

^bGeometric coefficients corresponded to initial value of surface curvature. (See appendix A.)

^cGeometric coefficients corresponded to final value of surface curvature for each specimen. (See appendix A.)

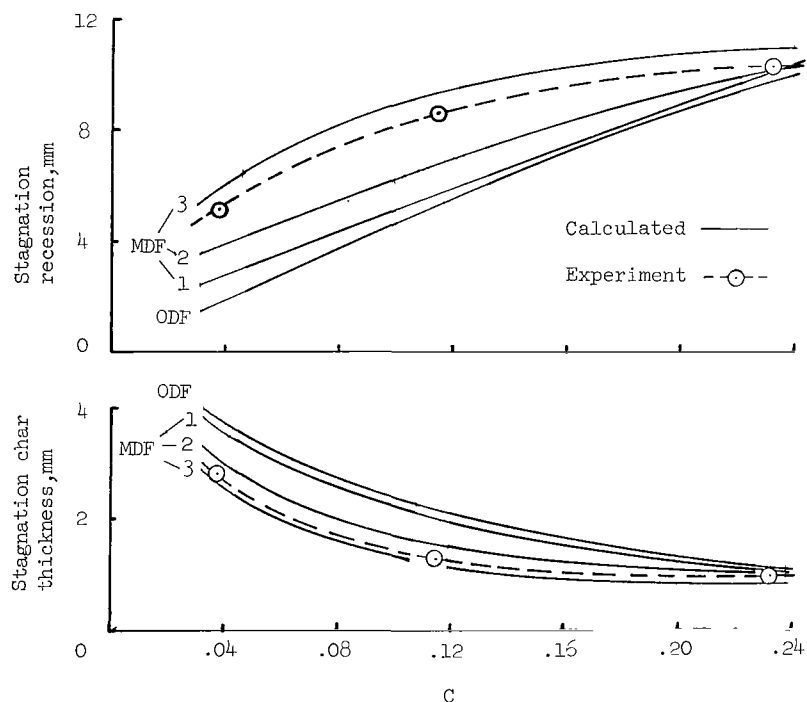


Figure 12.- Comparison of calculated and experimental performance of material A at a nominal stagnation pressure of 2.7 atmospheres.

determined stagnation recessions and char thicknesses for the three stream oxygen concentrations used. Also shown in figure 12 are solid curves which connect calculated results for each test condition. Char density and permeability values used for each material A calculation are tabulated in figure 12.

One-dimensional mass flow calculations.- Initial ablation calculations for material A considered one-dimensional mass flow (ODF) through the char layer. The results of these calculations are shown in figure 12. The char-density value tabulated in figure 12 and used for these computations was the same as that used in reference 7. The calculated oxygen concentration at the char surface was zero in all cases; thus, the oxidation process was governed by the diffusion of oxygen through the boundary layer. Therefore, the ODF recession results shown in figure 12 are the largest values that could be computed with this method. Note from the curves in figure 12 that reasonable agreement between calculation and test was obtained only for $C = 0.232$ (test in air). Thus, any subsequent MDF calculations should show significant improvement over the ODF calculations for $C = 0.038$ and 0.115 and still be in agreement for $C = 0.232$.

Multidimensional mass flow calculations.- Initial ablation calculations for material A considering multidimensional mass flow (MDF) through the char layer assumed, for convective blocking purposes, that the models retained their initial shape throughout the tests. The results of these calculations are shown as curve 1 in figure 12 and exhibit only a small improvement over the ODF results. However, the calculations predicted that inflow occurred throughout the test at $C = 0.038$ and that outflow was greatly reduced for $C = 0.115$. The pyrolysis gases (primarily hydrocarbons) are chemically cracked as they pass through the high-temperature regions of the char layer and deposit carbon. Inflow, or greatly diminished outflow, would reduce carbon deposition in the char layer and consequently, the density and permeability properties would be different from the values used in the curve 1 calculations at $C = 0.038$ and 0.115 . Therefore, more correct values for char density and permeability were obtained, as subsequently explained, for use in calculations at $C = 0.038$ and 0.115 .

The char density of specimen 9 (table II) was measured and found to be 214 kg/m^3 . Permeability of material A char in the same density range is reported in reference 8 to be $38 \times 10^{-11} \text{ m}^2$. However, this value was determined at room temperature after the char had experienced rapid cooling and resultant cracking to relieve thermal stresses and, consequently, probably was larger than actually existed during testing. Reducing this value to account for cracking in the same manner as was done in reference 7 yields $16 \times 10^{-11} \text{ m}^2$ as the estimated value of permeability for char with a density of 214 kg/m^3 .

These data were used to calculate the test results at $C = 0.038$ and 0.115 and are shown as curve 2 in figure 12. Although improved over previous efforts, the calculated recessions given by curve 2 were still significantly different from the experimental values.

Since all previous MDF calculations assumed that the char layer retained the original model shape throughout each test, curvature effects on convective blocking which occurred during the test were not considered. An estimate of these effects was obtained by using approximate geometric coefficients corresponding to the final value of surface curvature for each model considered. (See appendix A.) Using these approximate geometric coefficients and the same char properties as curve 2 resulted in the curve 3 predictions of material performance. Computed stagnation recessions, although slightly greater than the test values, produced the same shape curve as did the experimental data, and char-thickness predictions differed from the test measurements by an insignificant amount. Note from the curves in figure 12 that the ODF calculation and all MDF calculations for $C = 0.232$ predicted essentially the same values of recession and char thickness. The agreement of both ODF and MDF calculations with the experimental results at $C = 0.232$ occurred because the values of char permeability and thickness were sufficiently small to prevent convective blocking from being significantly reduced by MDF effects during this test.

The experimental results shown in figure 12 were bracketed by the MDF calculations which used char permeability values that were well within the limitations of recorded data. In all cases the computed oxygen concentration at the char surface was zero; thus the oxidation reaction was governed by diffusion of oxygen through the boundary layer. In such cases, oxygen diffusion through the boundary layer is governed solely by convective blocking. The results of MDF calculations shown in figure 12 indicate that multidimensional gas flow through the char layer can cause a sufficiently large reduction in convective blocking (and consequently, a large increase in oxygen diffusion) to affect ablation performance significantly.

Material B

The experimental results of material B at a stagnation pressure of 2.7 atmospheres are shown in figure 13 where stagnation-point recession is given for the three stream oxygen concentrations used. Also shown in figure 13 are results calculated with ODF and MDF methods. All calculations used a char density value of 272 kg/m^3 which was measured on material samples subjected to a high-enthalpy thermal environment. No char permeability data for material B were available. However, virgin material B was found to be over one order of magnitude less permeable than virgin material A (ref. 9). Therefore, material B char was estimated to have a permeability of approximately

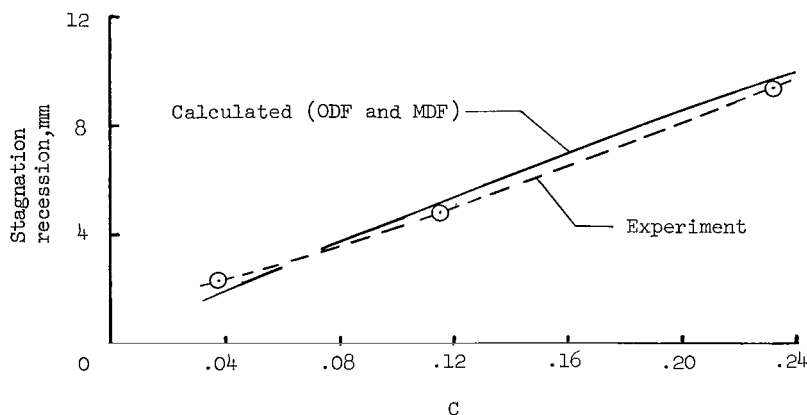


Figure 13.- Comparison of calculated and experimental performance of material B at a nominal stagnation pressure of 2.7 atmospheres.

$1 \times 10^{-11} \text{ m}^2$. Geometric coefficients for the MDF calculations corresponded to the final value of surface curvature for each test. The ODF and MDF calculations of material B recession differed by an insignificant amount and were reasonably close to the experimental values; therefore, convective blocking was not indicated to be significantly reduced by MDF effects at the test pressure level.

Flight Test

The flight performance of material A is analyzed in reference 7. However, some results of that analysis are presented herein to illustrate MDF effects on the performance of an actual flight nose cap. This nose cap, which had approximately the same shape as but was considerably larger than the ground-test specimen, is not believed to have undergone significant shape change during the flight test. Figure 14 shows the experimental pressure and calculated cold-wall laminar heating-rate distributions for the reference 7 nose cap. Local values of heating rate and pressure were approximately constant for $0 \leq \frac{s}{r_{\text{ref}}} < 0.6$. Because the nose cap of reference 7 was very blunt, it was assumed that the general solutions for a cylindrical char given previously herein were applicable. The nose cap pressure distribution shown in figure 14 was used to calculate mass flow behavior over the nose cap surface. The resulting mass flow distribution is shown in figure 15 for several values of t/R . As with the mass flow results for the flat-faced-cylinder pressure distribution, which are shown in figure 4, inflow into the stagnation region is low but increases as t/R increases. The point of maximum inflow occurs at $r/R \approx 0.65$ and outflow occurs for $r/R > 0.9$. A comparison of figure 15 with figure 4 shows the strong influence of pressure distribution on mass flow through the char surface. Both pressure distributions have approximately the same effect near the stagnation point, but the maximum inflow amplitudes shown in figure 4, which are

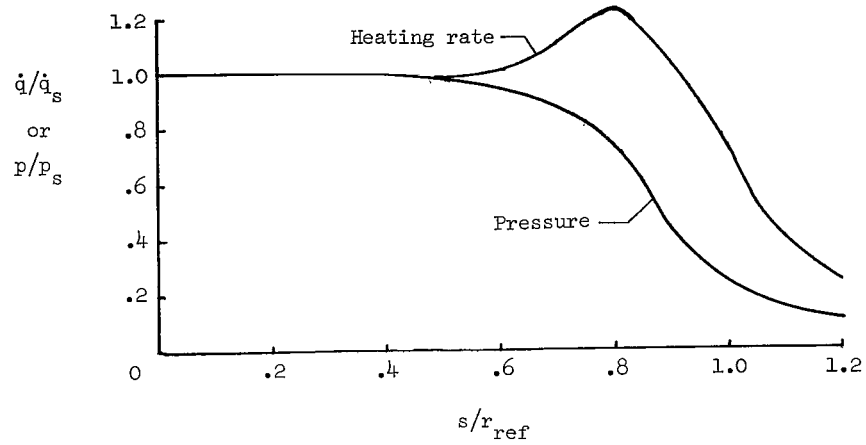


Figure 14.- Pressure and heating rate distributions for nose cap of reference 7.

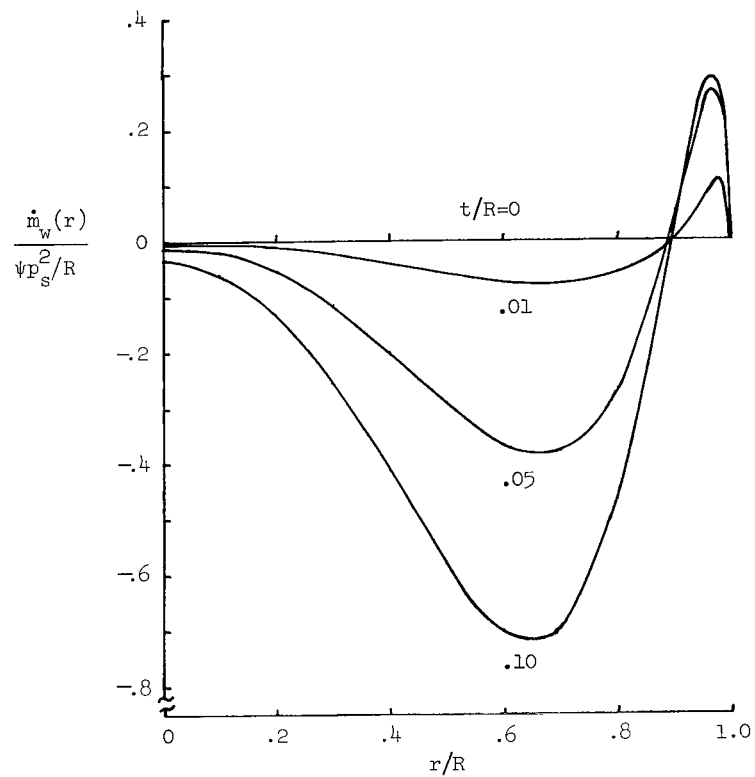


Figure 15.- Mass flow distribution at surface of cylindrical char layer resulting from external pressure distribution of figure 14.

associated with the flat-faced-cylinder pressure distribution, are considerably greater and occur farther outboard than the corresponding nose cap results shown in figure 15. This difference occurs because the nose cap pressure distribution does not decrease as abruptly near the edge $r = R$ as does the flat-faced-cylinder pressure distribution.

The nose cap final recession distribution was computed by both the ODF and MDF methods and is shown in figure 16. The ODF distribution curve is indicative of the result which would have been obtained by using any ablation computer program which embodies the assumption of one-dimensional mass transfer through the char layer. The MDF calculations, from which the final (end of flight) recession distribution in figure 16 was obtained, are shown in reference 7 to be in agreement with the recorded thermocouple and sensor data. The curves in figure 16 represent the difference between ODF and MDF methods because the stagnation recessions computed by both methods were equal.

Figure 17 shows the ratio of net aerodynamic heating computed by the MDF method to that computed by the ODF method for various meridional locations on the nose cap. It is seen from figure 17 that the effect of reduced convective blocking was to cause an increased diffusion of energy and oxygen through the boundary layer at off-stagnation locations, which resulted in the MDF recession distribution shown in figure 16. Note from figure 17 that the maximum aerodynamic heating, which is usually considered to occur at the time of peak cold-wall heating, occurs at the time of peak pressure when convective blocking is responsive to the pressure environment.

The increased diffusion rates of oxygen and energy through the boundary layer, resulting from decreased convective blocking, are characteristic of MDF effects. It has been demonstrated that these effects occurred in an actual flight test of material A and also occurred during ground ablation testing when material A was subjected to near

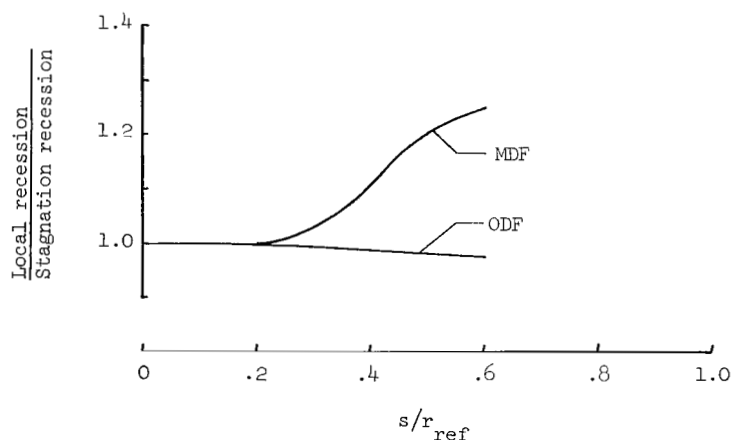


Figure 16.- Calculated final recession distributions for nose cap of reference 7.

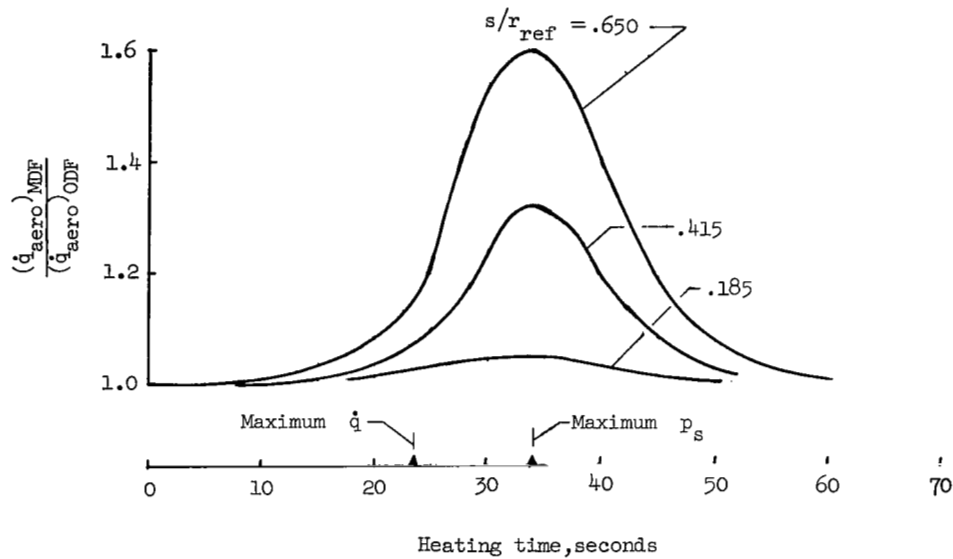


Figure 17.- Effect of reduced blocking on heating-rate history for nose cap of reference 7.

flight-level stagnation pressures. Analytical results given herein indicated that in a given environment, small specimens were more susceptible to these effects than larger ones. Consequently, subjecting small ground-test specimens to flight pressure levels could lead to different performance in the ground tests than would have occurred in flight on a much larger body. The manner in which ground specimens should be tested to compensate for size effects on convective blocking is discussed in the following section.

REPRODUCTION OF MATERIAL PERFORMANCE IN GROUND FACILITIES

Ground testing of ablation materials for flight application previously required investigators to select the most important flight environmental parameters, since it is impossible to reproduce the entire flight environment (p , h , and \dot{q}) for a small specimen in a ground facility. However, subjecting a ground-test specimen to flight heating and enthalpy levels results in reproducing a materials transient flight behavior only if convective blocking is also reproduced on the small model.

It is shown in appendix C that the ground test pressure required to reproduce flight heating on a small model at the flight enthalpy level, is also the same as that required to reproduce the flight convective-blocking history on the small model. This test pressure is given by

$$p_g = \frac{R_g}{R_f} p_f \quad (22)$$

where the subscripts g and f refer to ground test and flight, respectively. Since $R_g/R_f \ll 1$, the required ground test pressure is considerably less than flight pressure. Consequently, material performance is reproduced only if the surface removal reactions occurring in flight are independent of pressure. However, this condition does permit examination of the important cases of diffusion-controlled oxidation and melting.

CONCLUDING REMARKS

The analytical basis for multidimensional mass flow through a char layer has been presented. The mass flow of gases through the char surface has been shown to be significantly different, under certain conditions, from the one-dimensional assumption previously used. Comparison with both flight and ground experiments has shown, also, that consideration of multidimensional mass flow through the char layer resulted in a more accurate calculation of material performance than was previously possible. Based on the analytical and experimental results herein, the following conclusions are made:

1. For the same environmental conditions, ablation material, and geometry, convective blocking is more adversely affected on small ground-test specimens than on large flight vehicles solely because of body-size effects.

2. For the same environmental conditions, ablation material, and body size, convective blocking at the stagnation point is significantly reduced by increased surface curvature. Thus, hemispherical ground-test specimens are more susceptible to this effect at the stagnation point than flat-faced specimens.

3. For a given material, environment, and geometry, increases in char thickness during testing increase multidimensional flow through the char layer and may adversely affect material performance by decreasing convective blocking on the specimen.

4. Ground tests at flight pressure levels of materials which form highly permeable chars do not provide meaningful information concerning flight ablation performance since convective blocking is significantly reduced on small specimens.

5. A materials performance in a regime where surface reactions are independent of pressure can be reproduced in ground facilities on small specimens if the test pressure is properly reduced.

6. Because the qualitative analyses and calculations herein have shown that multidimensional gas flow through the char layer can have a significant effect on ablation performance, it is concluded that a more precise description of this physical mechanism is a basic requirement in the development of an accurate, multidimensional, analytical ablation model.

Langley Research Center,
National Aeronautics and Space Administration,
Langley Station, Hampton, Va., September 19, 1968,
124-07-01-34-23.

APPENDIX A

MODIFICATION OF ABLATION PROGRAM

An exact quantitative analysis of ablation performance considering multidimensional gas flow through the char layer requires a fundamental change in the mathematical model and development of a new ablation program. It was beyond the scope of work undertaken herein to develop this capability; therefore, an existing one-dimensional ablation routine was modified to incorporate the analytical results presented in this paper. The unmodified ablation program is based on the theory of reference 1.

In general, convective blocking at the surface of a charring ablator is due to gases generated at the surface (from oxidation and vaporization) and at the interface (from pyrolysis). All pyrolysis gases generated at the interface are considered in reference 1 to be injected into the boundary layer at the same location. Since a primary effect of multidimensional gas flow through the char layer is its influence on convective blocking, the analytical results herein were used to compute the mass flux of pyrolysis gases reaching the char surface at a given location instead of using the one-dimensional mass-transfer assumption. Mass flow at the surface of both the cylinder and hemisphere is given by an equation identical in form to

$$\dot{m}_w = \xi_1 \dot{m}_p - \xi_2 \frac{\psi p_s^2}{R} \quad (A1)$$

where ξ_1 and ξ_2 are geometry-dependent coefficients such as γ_1 and γ_2 or η_1 and η_2 . Equation (A1), however, does not account for differences in molecular weight of pyrolysis and stream gases. To account for the effect of molecular-weight differences on mass inflow at the char surface, equation (A1) was rewritten approximately as

$$\dot{m}_w = \psi \left(\frac{\xi_1 \dot{m}_p}{\psi_p} - \frac{\xi_2 p_s^2}{R} \right) \quad (A2)$$

The term in parentheses in equation (A2) represents the pressure gradient at the char surface. For positive values of this term, outflow occurs and a value of $\psi = \psi_p$ is used, in which case equation (A2) is identical with equation (A1). For negative values of this term, inflow occurs and a value of $\psi = \psi_{bl}$ is used.

Equation (A2) was combined with the ablation program based on the theory of reference 1 in the following manner. The pyrolysis gas flow rate \dot{m}_p appearing in the convective-blocking parameter in equation (13a) of reference 1 was replaced by equation (A2) of this report. The analytical model resulting from this modification retained the one-dimensional heat-transfer assumption, but for convective-blocking purposes assumed that multidimensional flow existed in the char layer.

APPENDIX A

The geometric coefficients ξ_1 and ξ_2 appearing in equation (A2) were evaluated at the stagnation point for a range of the char-thickness parameter t/R as described subsequently. The parenthetical term of equation (A2) was then evaluated as an instantaneous function of local char thickness, local pyrolysis rate, and external stagnation pressure. In this manner, the mass flow through the char surface at the stagnation point was evaluated in a quasi-steady manner and an approximate analysis of MDF effects on ablation was performed. In calculations of ablation performance, this modification neglected effects of shape change on convective blocking. Furthermore, this modification neglected the effects on convective blocking of instantaneous differences in pyrolysis rate and char thickness over the model since the analytical results given herein considered only char layers of uniform thickness subjected to a uniform pyrolysis mass injection distribution.

In order to examine the stagnation-area ablative performance of specimens with surface curvature between the extremes of a flat-faced cylinder and a hemisphere, approximate geometric coefficients ξ_1 and ξ_2 were generated by interpolating on the basis of surface area between stagnation values of the cylinder and hemisphere coefficients γ_1 and γ_2 and η_1 and η_2 , respectively. The resulting variation of ξ_1 and ξ_2 with a surface-curvature parameter α is shown in figure 18. Values of ξ_1 and ξ_2 from figure 18 at the appropriate value of α were used to compute the results shown in figures 12 and 13. The initial and final values of α for each of the models considered in figure 12 are shown in figure 18 to indicate approximately the effect which a change in shape during testing had on the geometric coefficients ξ_1 and ξ_2 .

APPENDIX A

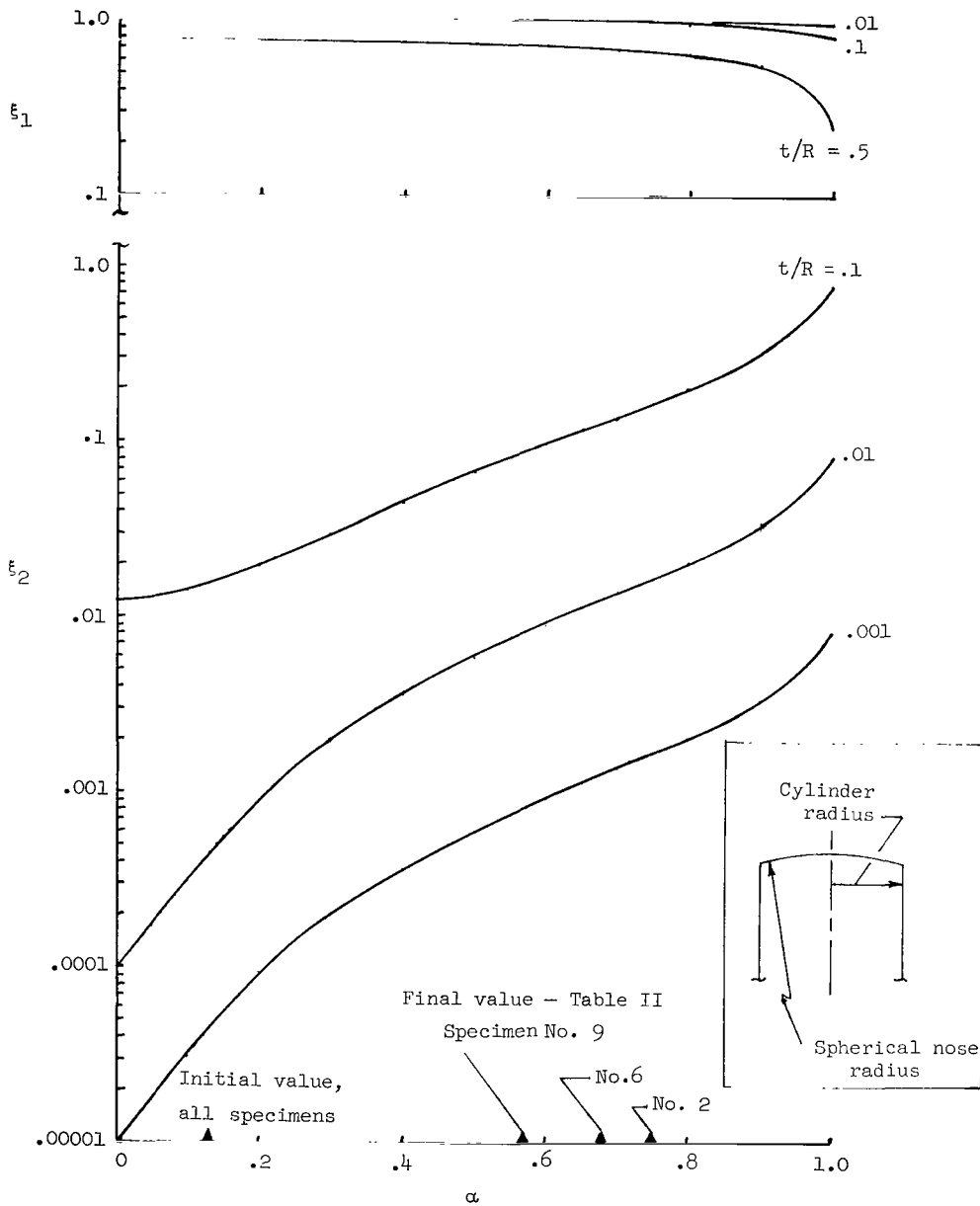


Figure 18.- Assumed variation of stagnation-point geometric coefficients with surface curvature (α = Cylinder radius/spherical nose radius) between limits of a flat-faced cylinder and a hemisphere.

APPENDIX B

EXPERIMENTAL PROGRAM

Two low-density phenolic-nylon materials were subjected to high-pressure thermal environments during ablation tests conducted at the Langley Research Center. The two materials, designated A and B, had the same basic composition and a bulk density of 553 kg/m^3 . Material A was molded with a process developed at the Langley Research Center; material B was molded by a commercial aerospace company with a different process. A characterization of both materials and details of the molding processes are given in reference 9. The only thermophysical material property which differed appreciably between the two materials was permeability. Phenolic Microballoons, contained in both virgin materials, were found to be fractured in material A, but were intact in material B. The increased permeability of material A was attributed to the fractured Microballoons.

Test Specimens and Conditions

The test specimen configuration is shown in figure 19. This blunted configuration was used because it provided a uniform cold-wall heating rate over a large part of the specimen surface.

The specimens were tested under supersonic flow conditions in oxygen concentrations between 2.9 and 23 percent (by mass) at four different pressure levels. The pressures and heating rates were determined experimentally with a probe and calorimeter, respectively, which had the same shape as the material specimens. The nominal environmental conditions at each pressure level were

p_s , atm	\dot{q} , MW/m ²	h , MJ/kg	τ_{\max} , kN/m ²
1.00	3.63	7.43	1.96
1.93	4.20	5.57	2.49
2.72	4.25	5.00	2.78
3.34	4.32	4.24	2.87

The shear stresses τ_{\max} shown were computed for smooth bodies with the initial specimen shape and do not indicate the actual shear stresses on the ablation specimen. However, they do provide reference values for the various test conditions and indicate that shear stresses were severe at all stagnation pressure levels.

APPENDIX B

Test Results

Characteristic post-test photographs of material A and material B are shown in figures 19 and 20, respectively. As test pressure was increased, both materials A and B underwent considerable shape change and the char thickness of both materials decreased. Since particulate material removal was not observed during testing, material recession was attributed to oxidation.

The complete experimental results for materials A and B are given in tables II and III and are compared in figure 21. The recession of both materials increased as either test pressure or oxygen concentration was increased; however for any given set of conditions, material A receded more than material B. In general, the char thickness of material A was less than or equal to that of material B. Inasmuch as material A char was more permeable than material B char, figure 21 is an experimental comparison of the actual effects of permeability on ablation performance. The results shown in figure 21 indicate that increased permeability has a deleterious effect on ablative performance because the material with the larger permeability receded more over the range of conditions shown.

It is noted that although ablation calculations of the 2.7-atmosphere tests of both materials were performed, it was not considered necessary to perform calculations of the other tests, since the experimental results at both higher and lower pressure levels followed trends similar to those for the 2.7-atmosphere tests.

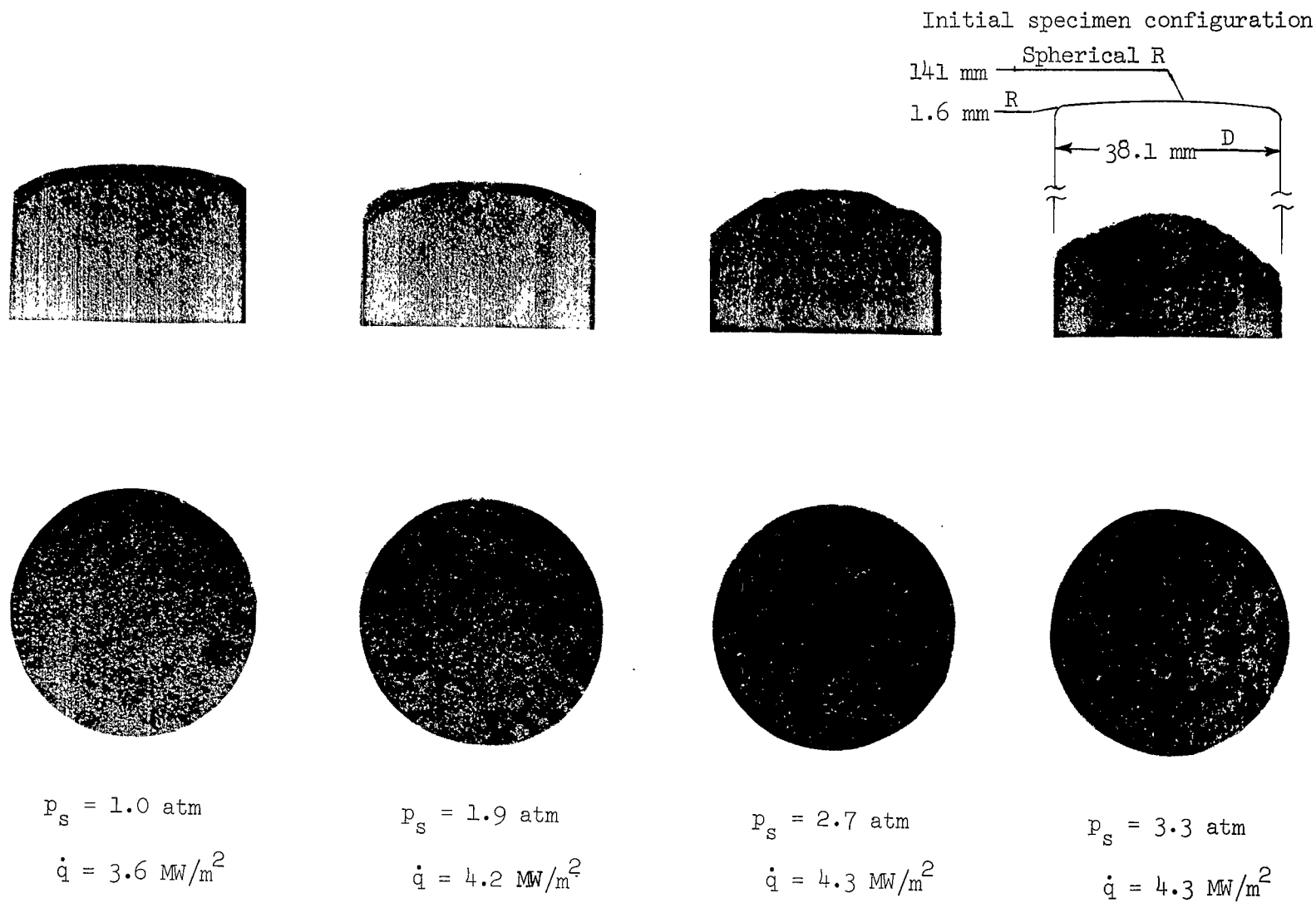
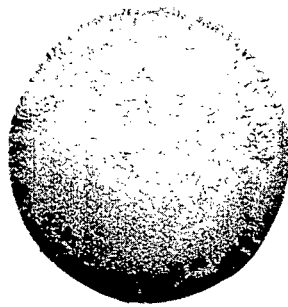
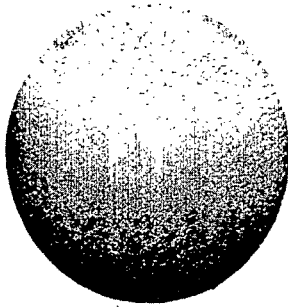
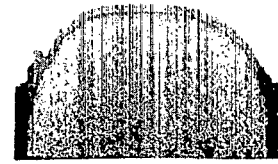
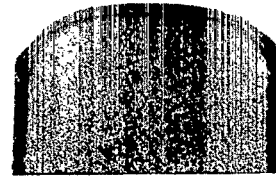
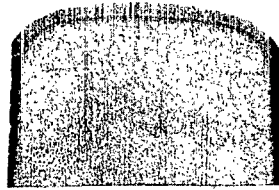
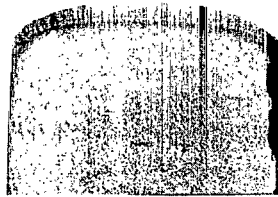


Figure 19.- Material A after 20 seconds exposure to various stagnation pressures and heating rates. $C = 0.115$. L-68-10,002



$$p_s = 1.0 \text{ atm}$$

$$\dot{q} = 3.6 \text{ MW/m}^2$$

$$p_s = 1.9 \text{ atm}$$

$$\dot{q} = 4.2 \text{ MW/m}^2$$

$$p_s = 2.7 \text{ atm}$$

$$\dot{q} = 4.3 \text{ MW/m}^2$$

$$p_s = 3.3 \text{ atm}$$

$$\dot{q} = 4.3 \text{ MW/m}^2$$

Figure 20.- Material B after 20 seconds exposure to various stagnation pressures and heating rates. $C = 0.115$. L-68-10,003

APPENDIX B

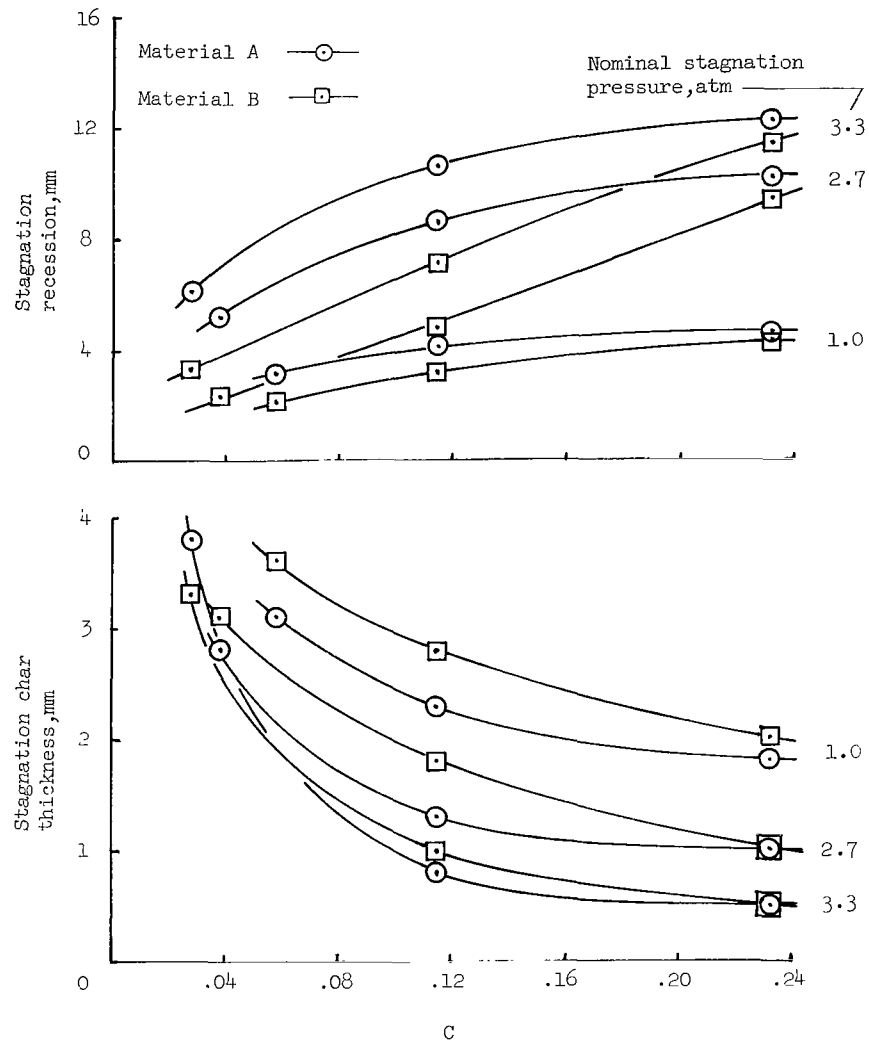


Figure 21.- Comparison of experimental performance of material A and material B.
Test duration, 20 seconds.

APPENDIX C

REPRODUCTION OF FLIGHT PERFORMANCE IN GROUND FACILITIES

Inasmuch as complete simultaneous reproduction of all flight environmental parameters in ground facilities on small models is not possible, ablation analysts must select those conditions which are considered most important. The fundamental relation between the environmental thermodynamic parameters can be shown (for example, ref. 1) to be

$$\dot{q} \propto h\sqrt{p/R} \quad (C1)$$

It is seen from the relation (C1) that reproducing the flight thermal environment (\dot{q} and h) on a small body will lead to the relation

$$p_g = \frac{R_g}{R_f} p_f \quad (C2)$$

where the subscripts g and f refer to ground test and flight, respectively. The ground test pressure given by equation (C2) is obviously less than flight since $R_g/R_f \ll 1$. Because of the absence of any analytical relationship between pressure and material performance, the degree of simulation with flight in any ground test could not be determined. However, the analytical results of this report show that a primary effect of pressure on material performance is its influence on convective blocking.

Reproduction of the transient flight behavior of an ablation material requires that the material-recession and char-thickness history be reproduced. Reproducing the flight thermal environment and stream composition in a ground facility accomplishes this requirement if the convective-blocking history which would occur in flight can be reproduced on the ground-test model. Thus, the problem becomes that of reproducing mass flow through the surface of both ground and flight bodies. Considering the stagnation point of a flat-faced cylinder and requiring mass flow equality from the surface of both flight- and ground-test bodies yields, from equation (12),

$$(\gamma_1 \dot{m}_p)_g - \left(\gamma_2 \frac{\psi p^2}{R} \right)_g = (\gamma_1 \dot{m}_p)_f - \left(\gamma_2 \frac{\psi p^2}{R} \right)_f \quad (C3)$$

The coefficient γ_1 , given by equation (13a), can be shown to be approximately equal to unity for $t/R < 0.25$. Since the pyrolysis rates \dot{m}_p are equal, equation (C3) becomes

$$\frac{p_g^2}{p_f^2} = \frac{R_g}{R_f} \frac{(\gamma_2)_f}{(\gamma_2)_g} \quad (C4)$$

APPENDIX C

The coefficient γ_2 , given by equation (13b), can also be expressed approximately for $t/R < 0.25$ as

$$\gamma_2 \propto t/R \quad (C5)$$

Combining equations (C4) and (C5) yields the governing relation for a flat-faced cylinder, which is

$$p_g = \frac{R_g}{R_f} p_f \quad (C6)$$

and is the same relation given in equation (C2). Thus, varying the ground-test pressure to reproduce the flight thermal environment on a flat-faced ground-test model also reproduces flight convective-blocking history and, consequently, material performance at the stagnation point whenever surface reactions are independent of pressure.

REFERENCES

1. Swann, Robert T.; Pittman, Claud M.; and Smith, James C.: One-Dimensional Numerical Analysis of the Transient Response of Thermal Protection Systems. NASA TN D-2976, 1965.
2. Eckert, E. R. G. (With Pt. A and Appendix by Robert M. Drake, Jr.): Heat and Mass Transfer. Second ed. of Introduction to the Transfer of Heat and Mass, McGraw-Hill Book Co., Inc., 1959.
3. Comm. on Metric Pract.: ASTM Metric Practice Guide. NBS Handbook 102, U.S. Dep. Com., Mar. 10, 1967.
4. Muskat, M.: The Flow of Homogeneous Fluids Through Porous Media. First ed., second printing, J. W. Edwards, Inc., 1946.
5. Beckwith, Ivan E.; and Cohen, Nathaniel B.: Application of Similar Solutions to Calculation of Laminar Heat Transfer on Bodies With Yaw and Large Pressure Gradient in High-Speed Flow. NASA TN D-625, 1961.
6. Beckwith, Ivan E.: Similar Solutions for the Compressible Boundary Layer on a Yawed Cylinder With Transpiration Cooling. NASA TR R-42, 1959. (Supersedes NACA TN 4345.)
7. Dow, Marvin B.; Bush, Harold G.; and Tompkins, Stephen S.: Analysis of the Supercircular Reentry Performance of a Low-Density Phenolic-Nylon Ablator. NASA TM X-1577, 1968.
8. Anon.: The Permeabilities of an Elastomer, a Low-Density Epoxy and a Low-Density Phenolic-Nylon Char. 8561-1728-6-IV (Contract NAS 1-5448), Southern Res. Inst., 1967.
9. Keller, L. B.: Development of Characterized and Reproducible Syntactic Foam of Phenolic Nylon for Heat Shields. Rep. No. P66-49 (Contract NAS 2-2739), Res. Develop. Div., Hughes Aircraft Co., 1965.

TABLE I.- THERMOPHYSICAL PROPERTIES OF LOW-DENSITY PHENOLIC-NYLON
[Values used are those from ref. 7]

Char:

Specific reaction-rate constant, $\text{kg}/\text{m}^2\text{-s-atm}$	First-order	4.9×10^{10}
Activation temperature, $^{\circ}\text{K}$	oxidation	42 500
Average emissivity		0.8
Specific heat, $\text{kJ}/\text{kg-}^{\circ}\text{K}$		2.26
Thermal conductivity, $\text{W}/\text{m-}^{\circ}\text{K}$, at temperature of -		
278 $^{\circ}$ K		0.16
833 $^{\circ}$ K		0.16
1110 $^{\circ}$ K		0.50
1390 $^{\circ}$ K		1.22
1670 $^{\circ}$ K		1.87
1940 $^{\circ}$ K		2.65
2220 $^{\circ}$ K		3.74
2500 $^{\circ}$ K		4.75
2780 $^{\circ}$ K		6.24
3050 $^{\circ}$ K		7.66

Virgin material:

Specific reaction-rate constant, $\text{kg}/\text{m}^2\text{-s-atm}$	7.74×10^6
Activation temperature, $^{\circ}\text{K}$	12 890
Effective heat of pyrolysis, MJ/kg	1.28
Density, kg/m^3	553
Specific heat, $\text{kJ}/\text{kg-}^{\circ}\text{K}$, at temperature of -	
311 $^{\circ}$ K	1.51
367 $^{\circ}$ K	1.80
423 $^{\circ}$ K	2.07
478 $^{\circ}$ K	2.24
533 $^{\circ}$ K	2.28
589 $^{\circ}$ K	2.28
Thermal conductivity, $\text{W}/\text{m-}^{\circ}\text{K}$, at temperature of -	
300 $^{\circ}$ K	0.080
390 $^{\circ}$ K	0.084
500 $^{\circ}$ K	0.088
610 $^{\circ}$ K	0.092
710 $^{\circ}$ K	0.094

Pyrolysis gases:

Effective specific heat, $\text{kJ}/\text{kg-}^{\circ}\text{K}$, at temperature of -	
278 $^{\circ}$ K	3.64
556 $^{\circ}$ K	3.64
833 $^{\circ}$ K	3.64
1000 $^{\circ}$ K	4.81
1112 $^{\circ}$ K	8.25
1168 $^{\circ}$ K	11.70
1390 $^{\circ}$ K	13.60
1555 $^{\circ}$ K	11.70
1668 $^{\circ}$ K	7.53
1810 $^{\circ}$ K	5.22
1945 $^{\circ}$ K	4.39
2220 $^{\circ}$ K	5.00
2780 $^{\circ}$ K	9.20
3330 $^{\circ}$ K	20.00

TABLE II.- MATERIAL A RESULTS
[20-second-tests]

Specimen	Stream composition *		p_s , atm	Stagnation recession, mm	Char thickness, mm
	O ₂	N ₂			
1	0.232	0.768	0.87	4.6	1.8
2	.232	.768	2.51	10.2	1.0
3	.232	.768	3.34	12.2	.5
4	.115	.885	1.00	4.1	2.3
5	.115	.885	1.93	6.6	1.8
6	.115	.885	2.72	8.6	1.3
7	.115	.885	3.34	10.7	.8
8	.058	.942	1.00	3.1	3.1
9	.038	.962	2.72	5.1	2.8
10	.029	.971	3.61	6.1	3.8

*Mass basis.

TABLE III.- MATERIAL B RESULTS
[20-second tests]

Specimen	Stream composition *		p_s , atm	Stagnation recession, mm	Char thickness, mm
	O ₂	N ₂			
1	0.232	0.768	0.96	4.3	2.0
2	.232	.768	2.51	9.4	1.0
3	.232	.768	3.34	11.4	.5
4	.115	.885	1.00	3.3	2.8
5	.115	.885	1.93	4.3	2.5
6	.115	.885	2.72	4.8	1.8
7	.115	.885	3.34	7.1	1.0
8	.058	.942	1.00	2.0	3.6
9	.038	.962	2.72	2.3	3.1
10	.029	.971	3.61	3.3	3.3

*Mass basis.

FIRST CLASS MAIL

010 011 50 01 305 68013 00903
AIR FORCE RESEARCH LABORATORY/AFWL/
KIRTLAND AIR FORCE BASE, NEW MEXICO 87117

ALL INFORMATION CONTAINED HEREIN IS UNCLASSIFIED

POSTMASTER: If Undeliverable (Section 151
Postal Manual) Do Not Return

"The aeronautical and space activities of the United States shall be conducted so as to contribute . . . to the expansion of human knowledge of phenomena in the atmosphere and space. The Administration shall provide for the widest practicable and appropriate dissemination of information concerning its activities and the results thereof."

— NATIONAL AERONAUTICS AND SPACE ACT OF 1958

NASA SCIENTIFIC AND TECHNICAL PUBLICATIONS

TECHNICAL REPORTS: Scientific and technical information considered important, complete, and a lasting contribution to existing knowledge.

TECHNICAL NOTES: Information less broad in scope but nevertheless of importance as a contribution to existing knowledge.

TECHNICAL MEMORANDUMS: Information receiving limited distribution because of preliminary data, security classification, or other reasons.

CONTRACTOR REPORTS: Scientific and technical information generated under a NASA contract or grant and considered an important contribution to existing knowledge.

TECHNICAL TRANSLATIONS: Information published in a foreign language considered to merit NASA distribution in English.

SPECIAL PUBLICATIONS: Information derived from or of value to NASA activities. Publications include conference proceedings, monographs, data compilations, handbooks, sourcebooks, and special bibliographies.

TECHNOLOGY UTILIZATION PUBLICATIONS: Information on technology used by NASA that may be of particular interest in commercial and other non-aerospace applications. Publications include Tech Briefs, Technology Utilization Reports and Notes, and Technology Surveys.

Details on the availability of these publications may be obtained from:

SCIENTIFIC AND TECHNICAL INFORMATION DIVISION
NATIONAL AERONAUTICS AND SPACE ADMINISTRATION
Washington, D.C. 20546